# Flutter Analysis with Stabilized Finite Elements based on the Linearized Frequency-domain Approach

Kevin E. Jacobson*, Bret K. Stanford†, Stephen L. Wood‡, and W. Kyle Anderson§
*NASA Langley Research Center, Hampton, VA, 23681*

**When designing and certifying aircraft, engineers must take into consideration aeroelastic effects such as flutter. Design and certification of a vehicle may require analysis of thousands of aeroelastic responses. Standard tools in the aerospace industry are based on linear aerodynamic models such as the doublet-lattice method, but these methods can be nonconservative in certain situations such as in the transonic regime. While computational fluid dynamics (CFD) is a higher fidelity alternative, the time-marching approach has a drastically increased computational cost compared to the linear aerodynamic methods. By taking advantage of the periodic nature of flutter, frequency-domain methods offer a more efficient alternative to time-marching CFD. In this work, a linearized frequency-domain method is implemented and verified in the stabilized finite-element solver in FUN3D. The linearized frequency-domain method is demonstrated and compared to other methods for traditional benchmark cases for computational aeroelasticity: the AGARD 445.6 wing, the Benchmark Supercritical Wing, and the Benchmark NACA 0012 Wing.**

## I. Introduction

Certification of flight vehicles is an expensive process requiring many flight tests in order to demonstrate the safety of a new aircraft or a modification to an existing aircraft. Reducing the time and cost of certification is of great interest to the aerospace industry. A central idea to reducing cost is certification by analysis where analyses, which can be based on computational modeling, wind tunnel data, or models from other flight tests, have the potential to replace new flight tests. An important part of certification by analysis is understanding and quantifying uncertainty of the results. Parametric uncertainty quantification required for high-fidelity aeroelastic models is a computationally expensive task due to the large number of variables and associated uncertainty that affect the aeroelastic characteristics of the vehicle [1]. Therefore, efficient high-fidelity modeling, which will allow many analyses with high accuracy and a reasonable computational cost, is of interest to those pursuing certification by analysis.

Efficient high-fidelity modeling is also of great interest to the field of multidisciplinary analysis and optimization (MDAO) where lower computational costs can push more accurate analysis tools earlier in the design process. More accurate analysis early in the design process is expected to lead to more confidence in designs and fewer costly late-stage modifications. Static aeroelastic optimization with the objective of maximizing the performance of an aircraft [2] leads to slender, flexible wings that are susceptible to unsteady aeroelastic effects such as flutter and gust loads. Therefore, aeroelastic constraints that account for these effects are important for these MDAO processes to produce realistic designs. While some researchers have demonstrated CFD-based flutter constraints in the time domain [3–6], these methods are computationally intensive due to the required length of temporal integration. This makes them difficult to apply to complex certification where thousands of scenarios may need to be analyzed or optimization problems where flutter constraints may need to be applied to a range of conditions and evaluated hundreds of times. Methods such as the linearized frequency-domain (LFD) [7, 8], harmonic balance [9, 10], and time-spectral method [11, 12] take advantage of the periodic nature of flutter to reduce the computational cost. For example, a typical time-marching flutter analysis will require a nonlinear static aeroelastic solution and multiple time-domain solutions with thousands of nonlinear time steps [13], whereas the linearized frequency-domain method requires the same nonlinear static aeroelastic solution but replaces the time-marching problems with tens or hundreds of linear systems to solve. In addition to rapid analysis, efficient computation of sensitivities for these methods is a key means to further reduction of the computational cost of uncertainty quantification or optimization.

---

*Research Aerospace Engineer, Aeroelasticity Branch, MS 340, AIAA Member, kevin.e.jacobson@nasa.gov
†Research Aerospace Engineer, Aeroelasticity Branch, MS 340, AIAA Associate Fellow.
‡Research Scientist, Computational Aerosciences Branch, MS 128, AIAA Member.
§Senior Research Scientist, Computational Aerosciences Branch, MS 128, AIAA Associate Fellow.

As a linearized method based on Reynolds-averaged Navier-Stokes (RANS) analysis, there are limitations to the applicability of the LFD method. RANS models are known to be inaccurate for flows with significant separation. The linearization about a nonlinear flow field in the method means that the method is not applicable to aeroelastic problems where nonlinearities are important beyond the static aeroelastic equilibrium, such as aeroelastic instability problems that are dependent on perturbation amplitude and many limit cycle oscillation problems.

This paper describes an implementation of the LFD approach in the Streamlined Upwind Petrov-Galerkin (SUPG) [14] finite-element solver in FUN3D. The LFD method and its application to a p-k flutter analysis is described. Verification of the implementation is presented as well as demonstration of the approach to the AGARD 445.6, the Benchmark Supercritical, and the Benchmark NACA 0012 Wings. Finally, some initial progress to adjoint-based sensitivities of the LFD method is described.

## II. Methodology

### A. Stabilized Finite Elements in FUN3D

FUN3D is a NASA Langley Research Center CFD code that has been applied to a wide range of aerospace analysis and design problems [15–18]. The primary discretization in FUN3D is a node-centered finite-volume solver, but in recent efforts [19, 20] a SUPG finite-element solver called FUN3D/SFE has been added. As discussed in more detail by Anderson et al. [19], the reasons for adding the alternate discretization are that the finite elements offer a viable path to higher-order CFD, it is easier to maintain linearizations for adjoint-based design and strong solvers due to the small stencil, and it provides improved accuracy on tetrahedral meshes. Although the finite-element method is capable of higher-order analysis, all of the results in this work are spatially second-order. For the frequency-domain analysis in this work, the underlying governing equations in the stabilized finite-element solver are the Reynolds-averaged Navier-Stokes equations with the negative Spalart-Allmaras turbulence model [21]. To account for mesh movement in aeroelastic problems, these equations are solved with an Arbitrary Lagrangian-Eulerian (ALE) formulation [20]:

$$\int_{\Omega(t)} (N + P)\left[\dot{\mathbf{q}} + \nabla \cdot (\mathbf{F} - \mathbf{q}\,\dot{\mathbf{x}}_G) + \mathbf{q}\nabla \cdot \dot{\mathbf{x}}_G - \mathbf{S}\right] d\Omega = 0, \tag{1}$$

where $N$ is the Galerkin weighting function, $P$ is the Petrov-Galerkin weighting function described by Anderson et al. [19], $\mathbf{q}$ is the flow state vector, $\mathbf{x}_G$ is the vector of volume mesh coordinates, $\mathbf{F}$ is the flux vector, and $\mathbf{S}$ is the source term. For aeroelastic analysis, dynamic grids in FUN3D/SFE are driven by the same mesh motion infrastructure as the finite-volume flow solver in FUN3D; therefore, the finite-element solver can be coupled to FUN3D's internal modal structural solver or tools like FUNtoFEM [22, 23], which provides a framework for coupled aeroelastic analysis and sensitivities.

### B. Linearized Frequency-domain Method

To derive the LFD method, the time-accurate governing equations of the flow, Eq. 1, are rewritten as

$$\mathbf{A}(\mathbf{q}, \dot{\mathbf{q}}, \mathbf{x}_G, \dot{\mathbf{x}}_G) = \mathbf{M}(\mathbf{q}, \mathbf{x}_G, \dot{\mathbf{x}}_G)\,\dot{\mathbf{q}} + \mathbf{R}(\mathbf{q}, \mathbf{x}_G, \dot{\mathbf{x}}_G) = 0, \tag{2}$$

where $\mathbf{M}$ is the mass matrix, which is a function of the state due to the Petrov-Galerkin weighting functions and $\mathbf{R}$ is the spatial residual for the flow problem. The time-dependent mesh and solution vectors are assumed to be an equilibrium state plus small perturbations: $\mathbf{x}_G = \mathbf{x}_{G0} + \bar{\mathbf{x}}_G(t)$, $\mathbf{q} = \mathbf{q}_0 + \bar{\mathbf{q}}(t)$. The governing equations of the flow are linearized about the equilibrium solution:

$$\mathbf{M}|_{\mathbf{x}_{G0},\mathbf{q}_0}\,\dot{\bar{\mathbf{q}}} + \left.\frac{\partial \mathbf{R}}{\partial \mathbf{q}}\right|_{\mathbf{x}_{G0},\mathbf{q}_0} \bar{\mathbf{q}} + \left.\frac{\partial \mathbf{R}}{\partial \mathbf{x}_G}\right|_{\mathbf{x}_{G0},\mathbf{q}_0} \bar{\mathbf{x}}_G + \left.\frac{\partial \mathbf{R}}{\partial \dot{\mathbf{x}}_G}\right|_{\mathbf{x}_{G0},\mathbf{q}_0} \dot{\bar{\mathbf{x}}}_G = 0. \tag{3}$$

Next, the small perturbations are assumed to be harmonic:

$$\bar{\mathbf{x}}_G(t) = \sum_{j=1}^{n} \hat{\mathbf{x}}_{G,j} e^{i\omega t}, \tag{4}$$

$$\bar{\mathbf{q}}(t) = \sum_{j=1}^{n} \hat{\mathbf{q}}_j e^{i\omega t}, \tag{5}$$

where $\hat{\mathbf{x}}_{G,j}$ and $\hat{\mathbf{q}}_j$ are Fourier coefficients. When these expressions are substituted into Eq. 3, the linearized frequency-domain equations can be simplified to:

$$\mathbf{A}_{LFD,j}\left(\mathbf{x}_{G0}, \mathbf{q}_0, \hat{\mathbf{x}}_{G,j}, \hat{\mathbf{q}}_j, \omega\right) = \left( i\omega\, \mathbf{M}\big|_{\mathbf{x}_{G0},\mathbf{q}_0} + \left.\frac{\partial \mathbf{R}}{\partial \mathbf{q}}\right|_{\mathbf{x}_{G0},\mathbf{q}_0} \right) \hat{\mathbf{q}}_j + \left.\frac{\partial \mathbf{R}}{\partial \mathbf{x}_G}\right|_{\mathbf{x}_{G0},\mathbf{q}_0} \hat{\mathbf{x}}_{G,j} + i\omega \left.\frac{\partial \mathbf{R}}{\partial \dot{\mathbf{x}}_G}\right|_{\mathbf{x}_{G0},\mathbf{q}_0} \hat{\mathbf{x}}_{G,j} = 0. \qquad (6)$$

This linear system is solved once for each frequency of interest ($\omega$) for each mesh motion input ($\hat{\mathbf{x}}_{G,j}$), which is computed by propagating the mode shapes of the structure through the CFD volume mesh motion process. The linear system is solved with a Generalized Minimum Residual (GMRES) method implemented in the Sparse Linear Algebra Toolkit (SLAT) [24]. From the resulting linearized flow and grid motion, Fourier coefficients $\hat{\mathbf{q}}_j$, oscillatory surface forces are computed as:

$$\hat{\mathbf{f}}_{a,j} = \left.\frac{\partial \mathbf{f}_a}{\partial \mathbf{q}}\right|_{\mathbf{x}_{G0},\mathbf{q}_0} \hat{\mathbf{q}}_j + \left.\frac{\partial \mathbf{f}_a}{\partial \mathbf{x}_G}\right|_{\mathbf{x}_{G0},\mathbf{q}_0} \hat{\mathbf{x}}_{G,j} + i\omega \left.\frac{\partial \mathbf{f}_a}{\partial \dot{\mathbf{x}}_G}\right|_{\mathbf{x}_{G0},\mathbf{q}_0} \hat{\mathbf{x}}_{G,j}, \qquad (7)$$

where $\mathbf{f}_a$ is the function to calculate aerodynamic surface forces.

The generalized aerodynamic forces (GAFs) can then be calculated by projecting the oscillatory surface forces onto the structure using the load transfer scheme. Alternatively, they can be computed using the mode shapes that have been projected onto the aerodynamic surface, $\mathbf{\Phi}_a$:

$$\mathbf{GAF}(\omega) = \mathbf{\Phi}_a^T \left[\hat{\mathbf{f}}_{a,1}, \hat{\mathbf{f}}_{a,2}, \ \dots, \hat{\mathbf{f}}_{a,n}\right]. \qquad (8)$$

Equations 6-8 are solved for a specified list of frequencies of interest. When GAFs are required at intermediate frequencies in the p-k flutter analysis, they are interpolated from the frequencies at which the LFD problem was solved.

### C. P-k Flutter Analysis Process

While the generalized aerodynamic forces generated by the linearized frequency-domain method can be utilized in various analyses, this section describes its application in a p-k flutter method. Figure 1 provides an overview of the process as currently implemented with FUN3D/SFE. Assuming the structure can be modeled with linear analysis, the first step is to perform a modal decomposition of structure. The resulting mode shapes $\mathbf{\Phi}$ are projected onto the aerodynamic surface, $\mathbf{\Phi}_a$, with a method such as radial basis function interpolation [25] or Matching-based Extrapolation of Loads and Displacements (MELD) [26]. After selecting an initial value of the dynamic pressure, the static aeroelastic problem is solved with FUN3D/SFE coupled to the modal structural solver. Next, the frequency-domain problem is solved and linearized about the static aeroelastic state, $q_\infty$, $\mathbf{x}_{G,0}$, $\mathbf{q}_0$ where $q_\infty$ represents the freestream dynamic pressure. Equation 6 is solved at selected frequencies, $\omega$, that cover the possible range of flutter frequencies. At each frequency, the linear system is solved for a perturbation of the mesh due to each structural mode. The elasticity-based volume mesh deformation in FUN3D [16, 17] propagates the modal surface displacements into the volume mesh to compute the mesh perturbations:

$$\mathbf{K}_G \hat{\mathbf{x}}_{G,j} = \mathbf{\Phi}_{a,j}, \qquad (9)$$

where $\mathbf{K}_G$ is the mesh deformation stiffness matrix and $\hat{\mathbf{x}}_{G,j}$ is the perturbation of the CFD mesh due to motion of mode $j$. After solving Eq. 6, the GAFs are found with Eq. 7 and Eq. 8. The GAFs are passed to a p-k flutter solver. In the p-k method, a flutter point is computed by solving the eigenvalue problem associated with the aeroelastic system. The solution has an exponential form $\bar{\xi}_j = \hat{\xi}_j e^{\nu_j t}$ where $\nu_j = \alpha_j + i\omega_j$. Writing the system in a state-space form leads to a nonlinear generalized eigenvalue problem:

$$\left[ \begin{pmatrix} \mathbf{I} & 0 \\ 0 & \mathbf{M} \end{pmatrix} \nu + \begin{pmatrix} 0 & -\mathbf{I} \\ \mathbf{K} - q\,\mathbf{GAF}(\omega) & \mathbf{C} \end{pmatrix} \right] \hat{\xi} = 0, \qquad (10)$$

where $\mathbf{M}$, $\mathbf{C}$, and $\mathbf{K}$ are the structural mass, damping, and stiffness matrices, respectively. A flutter dynamic pressure is found as a $q$ value that has a zero real part in the resulting eigenvalue. The computed flutter dynamic pressure is compared to freestream dynamic pressure in the static aeroelastic analysis, $q_\infty$. If these values are sufficiently different, the process is repeated with the computed flutter dynamic pressure as the freestream dynamic pressure. The cycle is executed until the dynamic pressure converges. This iterative approach is necessary since the GAFs are computed as

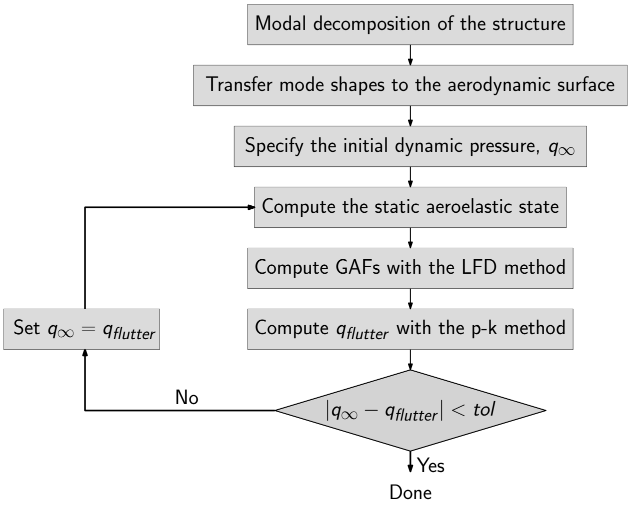

**Fig. 1 Flutter analysis process with the LFD and p-k methods.**

linearizations about the nonlinear static aeroelastic state that is affected by the dynamic pressure. This is particularly true in the transonic regime where the dynamic pressure can determine the position of a shock on the body, which can significantly influence the GAFs.

### D. Linearized Frequency-domain Verification

In order the set up the LFD problem, the linearizations of the residual with respect to mesh coordinates and velocities required for Eq. 6 are computed with operator overloading. This required modification to the existing operator overloading functionality in FUN3D/SFE to allow for differentiation with respect to variables other than the flow state. Therefore, the operator overloading extensions were verified by comparing directional derivatives computed with the operator overloading to complex step directional derivatives in Table 1. The linearizations in the table are about the turbulent flow over an NACA 64A010 airfoil at 0° angle of attack. The directions are randomly generated, and the derivatives in the table match to at least 13 digits indicating that the operator overloading is functioning properly.

The solution of the LFD problem was verified by comparing to small amplitude, forced-motion simulations in the time domain that approximate the linearized response. In the time-domain simulations, the perturbed structural mode was forced at a modal amplitude of 0.001 and at a selected reduced frequency, $k = \omega b / U_\infty$ where $b$ is the reference semichord length. The LFD problem was solved at the same reduced frequency. Once the time-domain solution reached a periodic state, a least-squares fit was applied to the flow state to compute the Fourier coefficients. The Fourier coefficients from the time domain were normalized by the motion amplitude in order to compare to the LFD results. Contours of the pressure coefficient Fourier coefficients computed from the time-domain and the LFD solution are presented in Fig. 2 for an inviscid NACA 64A010 airfoil undergoing plunge motion at Mach 0.6. The Fourier coefficients of the pressure coefficients match to the precision of the modal amplitude in the time-domain simulations.

The final step of verification was to compare the LFD GAFs from Eq. 8 to those determined from forced-motion time-domain simulations. This was done with the same approach as the flow solution verification with the least-squares fit applied to the modal force histories instead of the flow state histories. Table 2 gives the GAFs computed from the time-domain and the linearized frequency-domain at a transonic Mach number. In this table, $A_{ij}$ is the GAF representing the Fourier coefficient of the modal force in mode $i$ due to harmonic motion of mode $j$. As with the Fourier transformations of the flow states, the amplitude and phase of the GAFs match at least to the precision of the small-motion amplitude, 0.001, in the time-domain simulations.

**Table 1 Directional derivatives of the SFE residual.**

| | $\frac{\partial \mathbf{R}}{\partial \mathbf{x}_G}$ | $\frac{\partial \mathbf{R}}{\partial \dot{\mathbf{x}}_G}$ |
|---|---|---|
| Complex Step | 8.4087958908200**26**e+01 | 2.570533117129**395**e+00 |
| Operator Overloading | 8.4087958908200**12**e+01 | 2.570533117129**429**e+00 |

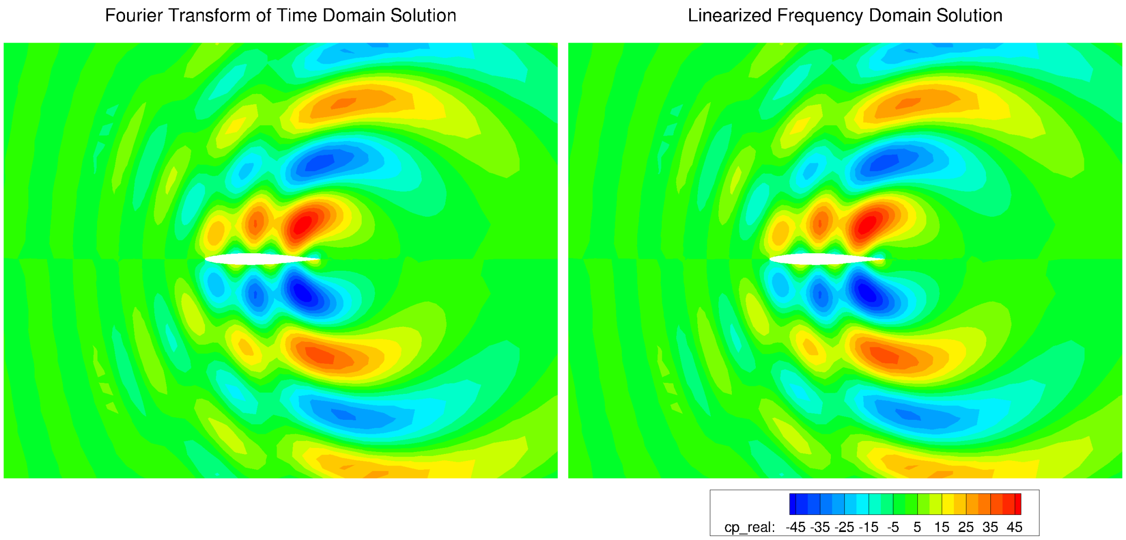

**(a) Real part.**

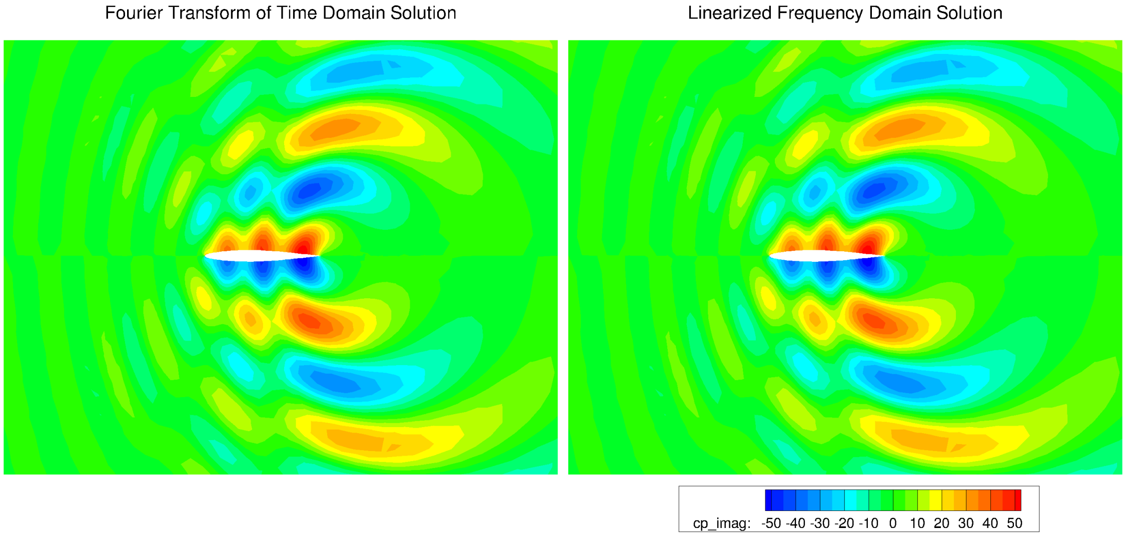

**(b) Imaginary part.**

**Fig. 2 Comparison of pressure coefficient Fourier coefficients computed from time-domain and linearized frequency-domain analysis. NACA 64A010, Mach=0.6, k=0.0837.**

**Table 2 Comparison of LFD GAFs to time-domain GAFs, NACA 64A010, Mach=0.85, k=0.1.**

| A11 | GAF value | Amplitude | Phase[°] |
|---|---|---|---|
| Time-domain least-squares fit | -0.062034714+0.009486982j | 0.062755945 | 171.305110883 |
| Linearized frequency-domain | -0.061998716+0.009479661j | 0.062719253 | 171.306750664 |
| A12 | GAF value | Amplitude | Phase[°] |
| Time-domain least-squares fit | 0.309573196-0.236955257j | 0.389850430 | -37.431369012 |
| Linearized frequency-domain | 0.309443029-0.236805496j | 0.389656042 | -37.425516008 |
| A21 | GAF value | Amplitude | Phase[°] |
| Time-domain least-squares fit | -0.003903398-0.020899123j | 0.021260523 | -100.579426188 |
| Linearized frequency-domain | -0.003914324-0.020910025j | 0.021273248 | -100.602961521 |
| A22 | GAF value | Amplitude | Phase[°] |
| Time-domain least-squares fit | 0.099903089+0.096984878j | 0.139236108 | 44.150842391 |
| Linearized frequency-domain | 0.099990495+0.096988284j | 0.139301207 | 44.126806007 |

## III. Results

### A. AGARD 445.6 Wing

The AGARD 445.6 wing [27] is a widely used benchmark problem for computational aeroelasticity. The wing that was tested at the NASA Langley Transonic Dynamics Tunnel (TDT) has an aspect ratio of 1.65, a 45° sweep angle, and 0.66 taper ratio. The airfoil is symmetric, and the wing has no twist. As discussed by Silva et al. [28], the wing has a thin airfoil, which means that the transonic regime is limited to Mach numbers very close to 1, and linear aerodynamic models that account for compressibility can effectively predict the subsonic aeroelastic behavior up to Mach numbers of about 0.98. Therefore, the subsonic aeroelastic response predicted by the LFD method should be comparable to that from Nastran's doublet-lattice method (DLM) [29]. Computations were performed with Nastran and FUN3D/SFE's LFD at two Mach numbers, 0.6 and 0.9. The FUN3D/SFE solver was run with the negative SA turbulence model active with a mesh consisting of 2.1 million nodes. Both the DLM and the LFD analyses were performed at the same reduced frequencies from $k = 0.001$ to $k = 1.0$. Figures 3 and 4 show the computed generalized aerodynamic forces from the two methods. Although there are some terms that are offset such as the real parts of A14 or A24 at both Mach numbers, the GAFs generally have similar values and variations as a function of reduced frequency. This demonstrates that the linearized frequency-domain CFD produces results comparable to linear aerodynamic models in flow regimes where the linear models are applicable.

### B. Benchmark Supercritical Wing

The Benchmark Supercritical Wing (BSCW) is the subject of the second Aeroelastic Prediction Workshop (AePW) [30]. The BSCW is a 16x32 inch rectangular wing with no twist or sweep and a SC(2)-0414 supercritical airfoil. Experiments were performed in the TDT with the wing mounted in a way such that it can be modeled as approximately rigid with springs at the root midchord that give the wing pitch and plunge degrees of freedom. The test case studied here is Case 2 from the second AePW, which is a flutter analysis at a Mach number of 0.74 and zero degrees angle of attack.

The coarse mixed-element node-centered mesh (3 million nodes) from the workshop-provided set of grids was analyzed with FUN3D/SFE. A steady simulation was run followed by a static aeroelastic analysis at the experimental flutter dynamic pressure of 168.80 psf. The LFD analysis was performed at 15 reduced frequencies ranging from $k = 0.001$ to $k = 0.08$ (the reduced frequency of the wind-off structural modes are 0.037 and 0.058). The corresponding root-locus plot from the p-k method is given in Fig. 5. The predicted flutter dynamic pressure is 152.95 psf. Figure 6 compares the damping predicted from the LFD GAFs generated at $q = 168.80$ psf to the FUN3D finite-volume time-domain solver [31]. With 30 linear system solves, the LFD results closely track the time-domain results over the

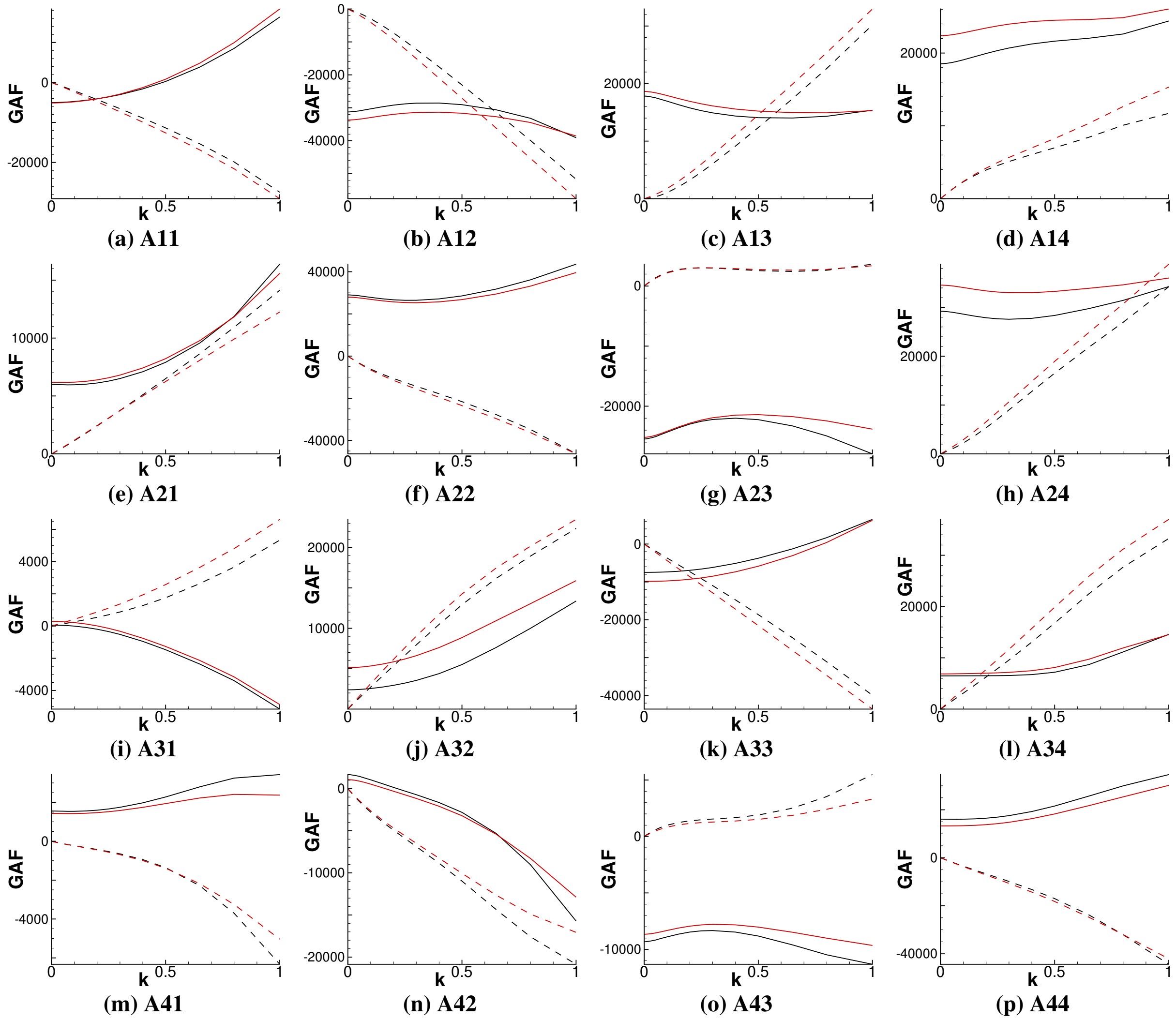

(a) A11 (b) A12 (c) A13 (d) A14

(e) A21 (f) A22 (g) A23 (h) A24

(i) A31 (j) A32 (k) A33 (l) A34

(m) A41 (n) A42 (o) A43 (p) A44

**Fig. 3 Generalized aerodynamic forces for the AGARD 445.6 wing at Mach=0.6. The black lines are the FUN3D/SFE LFD GAFs and the red lines are the Nastran DLM results. The solid and dashed lines are the real and imaginary parts, respectively.**

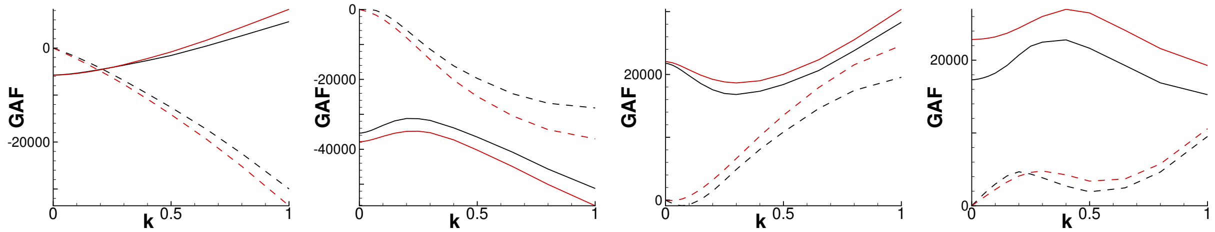

(a) A11 (b) A12 (c) A13 (d) A14

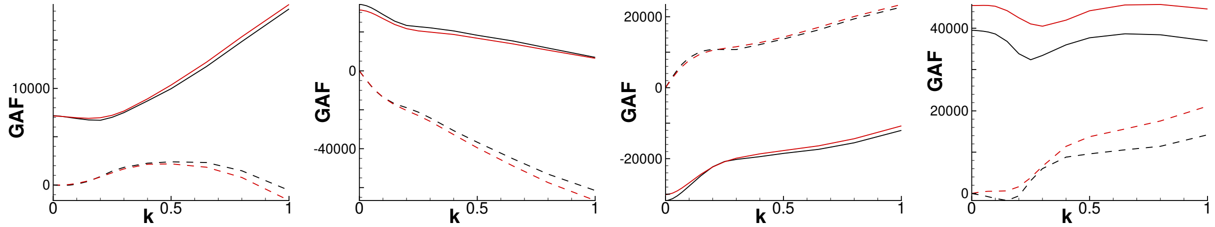

(e) A21 (f) A22 (g) A23 (h) A24

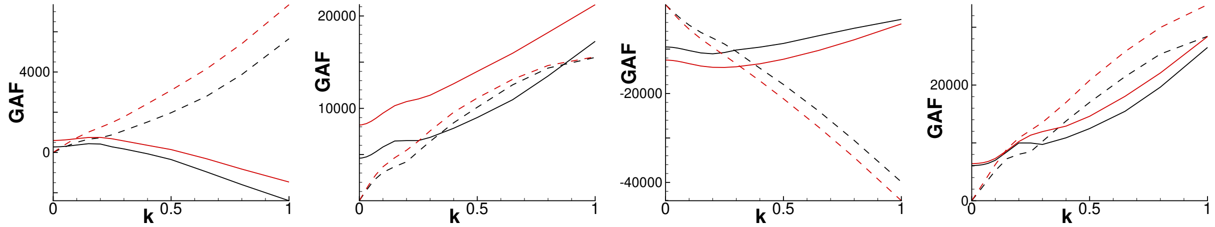

(i) A31 (j) A32 (k) A33 (l) A34

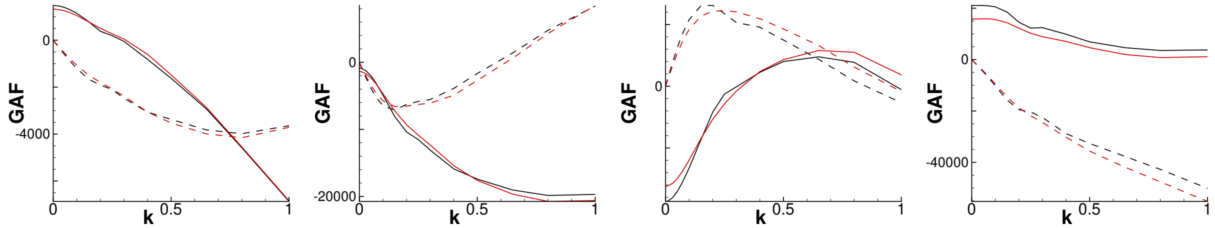

(m) A41 (n) A42 (o) A43 (p) A44

**Fig. 4** Generalized aerodynamic forces for the AGARD 445.6 wing at Mach=0.9. The black lines are the FUN3D/SFE LFD GAFs and the red lines are the Nastran DLM results. The solid and dashed lines are the real and imaginary parts, respectively.

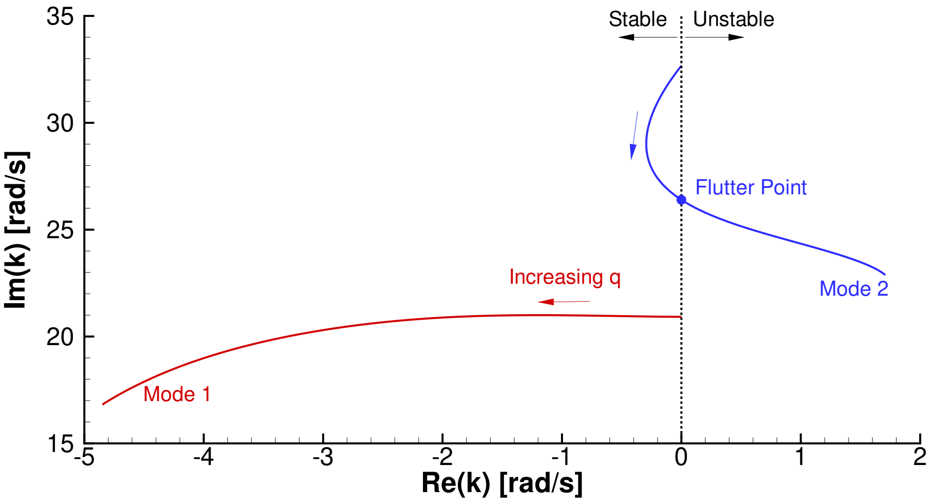

**Fig. 5 Root-locus plot for the Benchmark Supercritical Wing at Mach=0.74, AOA=0.0°. LFD analysis performed about $q_\infty$ =168.80 psf.**

entire range of dynamic pressure. On the finite-volume side, 9 time-domain problems were solved with each requiring thousands of nonlinear timesteps to simulate enough time-history to capture the stability. Near the peak damping at $q$ = 100 psf, the damping ratio predicted by LFD is within 0.6% of the time-domain value.

To continue the process described in Section II.C, the static aeroelastic and LFD analyses were rerun with $q$ = 152.95 psf. This led to a predicted flutter point of 152.72 psf, which is within 0.15% of the initial prediction. The flow at this condition is subsonic and one of the more benign cases from the AePW. Situations where the flow field is more dependent on the static aeroelastic dynamic pressure, such as a transonic problem, will require more iterations to converge (Fig. 1), than this case.

### C. Benchmark NACA 0012 Wing

The Benchmark NACA 0012 Wing is nominally identical to the BSCW from the previous section, with the exception that the supercritical airfoil of the BSCW is here replaced with a constant NACA 0012 airfoil lofted from the root to a rounded wingtip. Experimental flutter boundaries from the TDT are published in Ref. [32] and [33]. Computed flutter boundaries are shown in Fig. 7, for comparison with the experimental data, at an angle of attack of 0°. Three numerical data sets are shown: linear aeroelastic modeling with Nastran's DLM, viscous time-marching FUN3D simulations with the finite-volume solver, and viscous FUN3D/SFE using the LFD solver. The FUN3D results are computed on a coarse node-centered mesh with 3.7 million nodes.

The DLM-based flutter boundary is computed with a p-k solver, but is inaccurate at transonic Mach numbers. The time-marching results are able to capture the slight transonic flutter dip (minimum at Mach 0.76), but at a relatively high cost: the flutter point is not computed directly, as it would be with a p-k solver, but only bracketed. Time-marching simulations are conducted at progressively higher dynamic pressures, until an oscillatory growth in the time-history is observed. The LFD solutions, using the solution process in Fig. 1, return the flutter point directly and efficiently, and are moderately closer to the experimental data relative to the finite volume results. The iterative flutter process noted above is avoided here, since the case involves a symmetric airfoil at 0° angle of attack. The static aeroelastic result is therefore not a function of dynamic pressure.

### D. Computational Cost

While the previous sections highlight some of the additional types of information that can be extracted from the LFD results as compared to time-domain CFD, one of the primary motivations for implementing the LFD solver is to reduce the computational cost. Since the finite-element solver is slower than the finite-volume solver for time-domain analysis, and the workhorse for aeroelasticity with FUN3D is currently the finite-volume solver in the time-domain, computational cost of LFD is compared to the time-domain finite-volume solver. For the BSCW case with two mode shapes and 15 reduced frequencies of interest, the FUN3D/LFD requires 5.3 hours to perform the LFD analysis with 400 cores of Intel

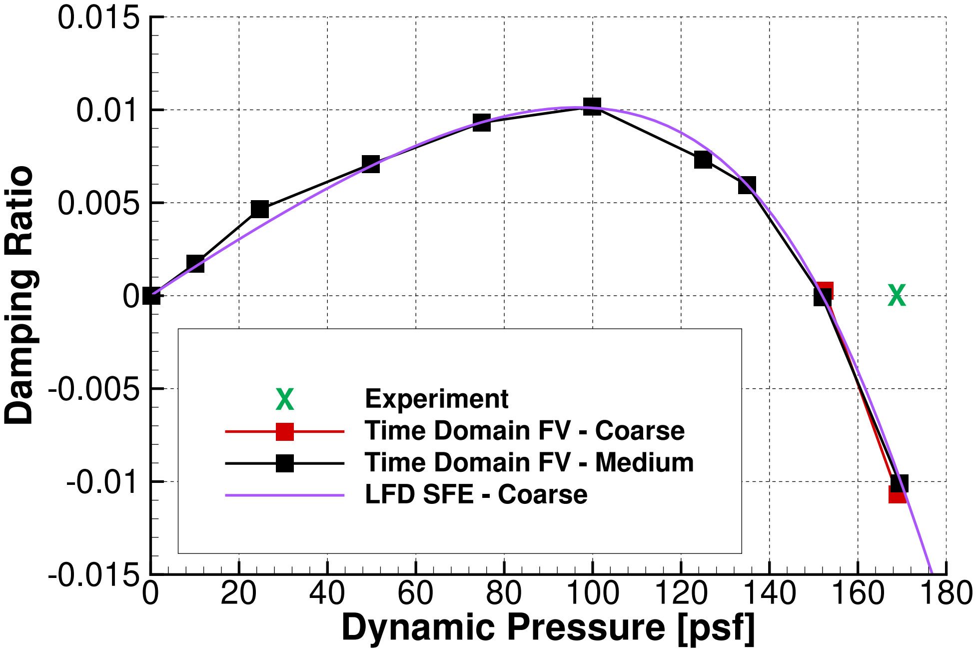

**Fig. 6 Predicted damping ratio of the Benchmark Supercritical Wing at Mach=0.74, AOA=0.0°. LFD analysis performed about $q_\infty$ =168.80 psf.**

Skylake processors. For a time-domain simulation, it requires at least 15,000 timesteps of the finite-volume solver to model the initial transients and generate a long enough time-history to identify the longer term trends of the damping in the system. With 400 Skylake cores, simulating 15,000 timesteps requires 37.5 hours of walltime. In the context of flutter analysis for more realistic aerospace configurations, there are several factors that would affect the relative cost of the two methods. The required number of linear solves in the LFD approach is proportional to the number of structural modes and reduced frequencies of interest. For the time-domain approach, the required number of timesteps is dependent on the necessary step size required for sufficient temporal resolution and the necessary total time record length to observe the response of the lowest frequency modes. Additionally, the required number of pseudotime subiterations per timestep also impacts the cost. Another consideration with both solvers is the required number of dynamic pressures to be analyzed to converge the process in Fig. 1 or sufficiently bracket the flutter point in the time-domain. Taking all of these factors into account for the NACA 0012 Wing, it was determined that the generation of the flutter boundary in Fig. 7 is at least ten times faster with the LFD method than the time-domain finite volume solver in FUN3D.

These comparisons have been performed without an effort dedicated to optimize the LFD code beyond the initial implementation. Applying a more sophisticated GMRES solver such as those discussed by Xu et al. [34] could reduce the time spent solving the linear system, which accounts for between 50% to 80% of the cost per linear problem. The majority of the remaining cost is the linearizations of the residual in forming the linear problem. In the current implementation, the solver is run with complex double-precision numbers throughout the code during the LFD phase. However, the linearizations are determined about a real-valued solution from the static aeroelastic problem, and therefore, they could be performed with real double-precision variables, which would reduce their cost by a factor between 2 and 3 with no loss is accuracy.

## IV. Linearized Frequency-domain Adjoint

As described in the introduction, two of the intended applications of the LFD solver are uncertainty quantification and MDAO. Both of these applications benefit from efficient computation of sensitivities that can be determined by solving the adjoint problem associated with the analysis. The fully coupled adjoint problem contains many of the terms that have already been implemented and verified as part of development of the static and time-domain aeroelastic adjoint equations [23]. However, because the residual of the LFD method, Eq. 6, is a linearization of the Navier-Stokes equations, the adjoint equations for this problem require second derivatives of the Navier-Stokes equations. Since

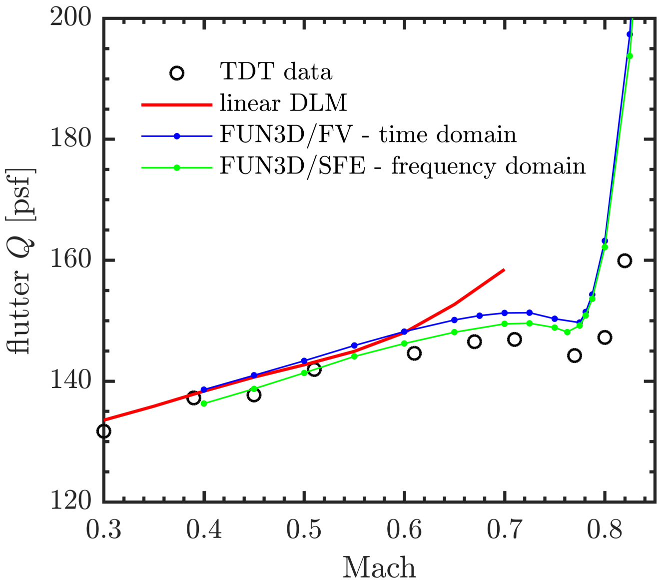

**Fig. 7 Flutter boundary of the Benchmark NACA 0012 Wing, for a nominal angle of attack of 0°.**

second derivatives of CFD residuals are not typically computed, in this section, terms related to these second derivatives are derived and tested on a small nonlinear problem to ensure that the present method will be practical to implement in the CFD solver. The adjoint terms related to the flow LFD problem can be computed from the following Lagrangian:

$$\begin{aligned}\mathcal{L}\left(\mathbf{x}, \mathbf{x}_{G0}, \hat{\mathbf{x}}_G, \mathbf{q}_0, \hat{\mathbf{q}}\right) = & f\left(\mathbf{x}, \mathbf{x}_{G0}, \hat{\mathbf{x}}_G, \mathbf{q}_0, \hat{\mathbf{q}}, \mathbf{u}_{A0}, \hat{\mathbf{u}}_A\right) \\ & + \psi_{G0}^T \mathbf{G}_0\left(\mathbf{x}, \mathbf{x}_{G0}, \mathbf{u}_{A0}\right) + \psi_{A0}^T \mathbf{A}_0\left(\mathbf{x}, \mathbf{x}_{G0}, \mathbf{q}_0\right) \\ & + \psi_G^T \mathbf{G}_{LFD}\left(\mathbf{x}, \hat{\mathbf{x}}_G, \hat{\mathbf{u}}_A\right) + \psi_A^T \mathbf{A}_{LFD}\left(\mathbf{x}, \mathbf{x}_{G0}, \hat{\mathbf{x}}_G, \mathbf{q}_0, \hat{\mathbf{q}}\right) \\ & = 0,\end{aligned} \tag{11}$$

where $f$ is the function of interest, $\mathbf{G}_0$ and $\mathbf{A}_0$ are the static aeroelastic volume mesh deformation and flow residuals, $\mathbf{G}_{LFD}$ is the mesh deformation residual related to the oscillatory motion input, and $\mathbf{u}_{A0}$ and $\hat{\mathbf{u}}_A$ are the static aeroelastic surface displacement and perturbations, respectively. From Eq. 2, the static flow residual simplifies to $\mathbf{A}_0 = \mathbf{R}$. Setting the partial derivatives of the Lagrangian with respect to the various state vectors to zero (the Karush-Kuhn-Tucker conditions [35, 36]) leads to the adjoint equations:

$$\left[\frac{\partial \mathbf{A}_{LFD}}{\partial \hat{\mathbf{q}}}\right]^T \psi_A = -\left[\frac{\partial f}{\partial \hat{\mathbf{q}}}\right]^T, \tag{12}$$

$$\left[\frac{\partial \mathbf{G}_{LFD}}{\partial \hat{\mathbf{x}}_G}\right]^T \psi_G = -\left[\frac{\partial f}{\partial \hat{\mathbf{x}}_G}\right]^T - \left[\frac{\partial \mathbf{A}_{LFD}}{\partial \hat{\mathbf{x}}_G}\right]^T \psi_A, \tag{13}$$

$$\left[\frac{\partial \mathbf{A}_0}{\partial \mathbf{q}_0}\right]^T \psi_{A0} = -\left[\frac{\partial f}{\partial \mathbf{q}_0}\right]^T - \left[\frac{\partial \mathbf{A}_{LFD}}{\partial \mathbf{q}_0}\right]^T \psi_A, \tag{14}$$

$$\left[\frac{\partial \mathbf{G}_0}{\partial \mathbf{x}_{G0}}\right]^T \psi_{G0} = -\left[\frac{\partial f}{\partial \mathbf{x}_{G0}}\right]^T - \left[\frac{\partial \mathbf{A}_0}{\partial \mathbf{x}_{G0}}\right]^T \psi_{A0} - \left[\frac{\partial \mathbf{A}_{LFD}}{\partial \mathbf{x}_{G0}}\right]^T \psi_A. \tag{15}$$

The terms related to the aerodynamic LFD residual in these equations are:

$$\left[\frac{\partial \mathbf{A}_{LFD}}{\partial \hat{\mathbf{q}}}\right] = i\omega \mathbf{M} + \frac{\partial \mathbf{R}}{\partial \mathbf{q}}, \tag{16}$$

$$\left[\frac{\partial \mathbf{A}_{LFD}}{\partial \hat{\mathbf{x}}_G}\right] = \frac{\partial \mathbf{R}}{\partial \mathbf{x}_G} + i\omega \frac{\partial \mathbf{R}}{\partial \dot{\mathbf{x}}_G}, \tag{17}$$

$$\begin{aligned}\left[\frac{\partial \mathbf{A}_{LFD}}{\partial \mathbf{q}_0}\right] =& \frac{\partial}{\partial \mathbf{q}}\left(i\omega \mathbf{M}\hat{\mathbf{q}}\right) + \frac{\partial}{\partial \mathbf{q}}\left(\frac{\partial \mathbf{R}}{\partial \mathbf{q}}\hat{\mathbf{q}}\right) \\ &+ \frac{\partial}{\partial \mathbf{q}}\left(\frac{\partial \mathbf{R}}{\partial \mathbf{x}_G}\hat{\mathbf{x}}_G\right) + \frac{\partial}{\partial \mathbf{q}}\left(i\omega\frac{\partial \mathbf{R}}{\partial \dot{\mathbf{x}}_G}\hat{\mathbf{x}}_G\right),\end{aligned} \tag{18}$$

$$\begin{aligned}\left[\frac{\partial \mathbf{A}_{LFD}}{\partial \mathbf{x}_{G0}}\right] =& \frac{\partial}{\partial \mathbf{x}_G}\left(i\omega \mathbf{M}\hat{\mathbf{q}}\right) + \frac{\partial}{\partial \mathbf{x}_G}\left(\frac{\partial \mathbf{R}}{\partial \mathbf{q}}\hat{\mathbf{q}}\right) \\ &+ \frac{\partial}{\partial \mathbf{x}_G}\left(\frac{\partial \mathbf{R}}{\partial \mathbf{x}_G}\hat{\mathbf{x}}_G\right) + \frac{\partial}{\partial \mathbf{x}_G}\left(i\omega\frac{\partial \mathbf{R}}{\partial \dot{\mathbf{x}}_G}\hat{\mathbf{x}}_G\right),\end{aligned} \tag{19}$$

where all of the partial derivatives are evaluated at the static aeroelastic solution, $\mathbf{x}_{G0}, \mathbf{q}_0$. The fact that only matrix-vector products are needed from all of the second derivative partials can be applied advantageously. The products have the form of a directional derivative of the first-order derivatives in the direction of the vector that it is multiplying by. For example,

$$\left.\frac{\partial}{\partial \mathbf{q}}\frac{\partial \mathbf{R}}{\partial \mathbf{q}}\right|_{\mathbf{q}_0} \hat{\mathbf{q}}, \tag{20}$$

can be thought of as the derivative of $\frac{\partial \mathbf{R}}{\partial \mathbf{q}}$ with respect to $\mathbf{q}$ in the direction of $\hat{\mathbf{q}}$. Rather than computing these second-order partial derivatives analytically, directional finite-difference derivatives can be used. Furthermore, because all of the first-order partial derivatives are real-valued, complex-step directional derivatives allow the linearization to be done within machine accuracy:

$$\left.\frac{\partial}{\partial \mathbf{q}}\frac{\partial \mathbf{R}}{\partial \mathbf{q}}\hat{\mathbf{q}}\right|_{\mathbf{q}_0} \approx \frac{\operatorname{imag}\left(\left.\frac{\partial \mathbf{R}}{\partial \mathbf{q}}\right|_{\mathbf{q}_0 + ih\ \operatorname{real}(\hat{\mathbf{q}})}\right)}{h} + i\,\frac{\operatorname{imag}\left(\left.\frac{\partial \mathbf{R}}{\partial \mathbf{q}}\right|_{\mathbf{q}_0 + ih\ \operatorname{imag}(\hat{\mathbf{q}})}\right)}{h}, \tag{21}$$

where $h$ is the complex-step size, which can be very small ($10^{-30}$-$10^{-50}$). The order of the differentiation can be switched so that the vector is always the same size as the second derivative allowing the directional finite-difference approach to be done. For example,

$$\left.\frac{\partial}{\partial \mathbf{x}_G}\frac{\partial \mathbf{R}}{\partial \mathbf{q}}\right|_{\mathbf{q}_0} \hat{\mathbf{q}} = \left.\frac{\partial}{\partial \mathbf{q}}\frac{\partial \mathbf{R}}{\partial \mathbf{x}_G}\right|_{\mathbf{q}_0} \hat{\mathbf{q}}. \tag{22}$$

This approach is verified with an arbitrary set of three nonlinear equations representing Eq. 2, i.e., the representative problem has residuals $\mathbf{A}_0$ and $\mathbf{A}_{LFD}$. The adjoint-based sensitivities are compared to real-valued finite difference derivatives in Table 3. The table also compares the sensitivities from LFD method to an adjoint result for a harmonic balance method where the input motion to the harmonic balance method is a complex-step input to get the same linearized response as the LFD approach. The two adjoint methods match to machine precision and also show at least six digits of agreement with the finite difference results. This example demonstrates that the sensitivities of the linearized frequency-domain method are able to be computed without analytically calculating the second partial derivatives of the flow residual. In future work, this method will be applied to the full CFD solver.

## V. Conclusions

In this work, a linearized frequency-domain method was added to the stabilized finite-element solver in FUN3D. The terms of the linearized frequency-domain problem were verified with a complex step derivative, and the frequency-domain solution was verified against small-amplitude forced motion simulations in the time-domain. Application of the method to the AGARD 445.6 wing produced generalized aerodynamic forces comparable to a linear aerodynamic model in flow regimes where linear modeling is applicable. For the Benchmark Supercritical Wing and the Benchmark NACA 0012 Wing in subsonic and transonic conditions, the aeroelastic response predictions from the LFD solver were nearly

**Table 3 Verification of adjoint-based sensitivities with an arbitrary nonlinear system.**

| Design Variable | 1 | 2 | 3 |
|---:|---|---|---|
| LFD Adjoint | 0.4245614128144636 | -0.1648677719451322 | 0.086271224971636**80** |
| HB Adjoint with complex-step $\mathbf{x}_G$ | 0.4245614128144636 | -0.1648677719451322 | 0.086271224971636**79** |
| LFD finite difference ($10^{-7}$) | 0.424561**3716147289** | -0.16486777**27672520** | 0.0862712**3571081086** |
| LFD finite difference ($10^{-8}$) | 0.4245614**082520887** | -0.16486777**49876981** | 0.0862712**3460058783** |
| LFD finite difference ($10^{-9}$) | 0.4245614**970699307** | -0.1648677**860899283** | 0.086271**10137382486** |

identical to time-domain RANS calculations but at a reduced computational cost. The capability to deliver accurate aeroelastic response predictions with greater efficiency is an important enabler of vehicle optimization and uncertainty quantification problems in MDAO and certification by analysis.

## Acknowledgments

This work is supported by the Transformational Tools and Technologies (TTT) project of the NASA Transformative Aeronautics Concepts Program (TACP).

## References

[1] Beran, P., Stanford, B., and Schrock, C., “Uncertainty Quantification in Aeroelasticity,” *Annual Review of Fluid Mechanics*, Vol. 49, 2017, pp. 361–386.

[2] Kenway, G. K. W., and Martins, J. R. R. A., “Multipoint High-Fidelity Aerostructural Optimization of a Transport Aircraft Configuration,” *Journal of Aircraft*, Vol. 51, No. 1, 2014, pp. 144–160.

[3] Palaniappan, K., Sahu, P., Alonso, J., and Jameson, A., *Active Flutter Control using an Adjoint Method*, American Institute of Aeronautics and Astronautics, 2006.

[4] Mani, K., and Mavriplis, D. J., “Adjoint-Based Sensitivity Formulation for Fully Coupled Unsteady Aeroelasticity Problems,” *AIAA Journal*, Vol. 47, No. 8, 2009, pp. 1902–1915.

[5] Zhang, Z., Wang, Q., Chen, P.-C., Yang, S., and Wang, Z., *CFD-based Aeroelastic Adjoint Sensitivities for Flight Vehicle Weight Minimization Using Sizing and Shape Design Variables*, American Institute of Aeronautics and Astronautics, 2017.

[6] Jacobson, K. E., Kiviaho, J. F., Kennedy, G. J., and Smith, M. J., “"Evaluation of Time-domain Damping Identification Methods for Flutter-constrained Optimization",” *Journal of Fluids and Structures*, Vol. 87, 2019, pp. 174 – 188.

[7] Widhalm, M., Dwight, R. P., Thormann, R., and Hübner, A., “Efficient Computation of Dynamic Stability Data with a Linearized Frequency Domain Solver,” *Proceedings of the European Conference on Computational Fluid Dynamics*, Lisbon, Portugal, 2010.

[8] Widhalm, M., and Thormann, R., *Efficient Evaluation of Dynamic Response Data with a Linearized Frequency Domain Solver at Transonic Separated Flow Condition*, 2017.

[9] Hall, K. C., Thomas, J. P., and Clark, W. S., “Computation of Unsteady Nonlinear Flows in Cascades Using a Harmonic Balance Technique,” *AIAA Journal*, Vol. 40, No. 5, 2002, pp. 879–886.

[10] Thomas, J. P., Dowell, E. H., and Hall, K. C., “Modeling Viscous Transonic Limit Cycle Oscillation Behavior Using a Harmonic Balance Approach,” *Journal of Aircraft*, Vol. 41, No. 6, 2004, pp. 1266–1274.

[11] Gopinath, A., and Jameson, A., “Time Spectral Method for Periodic Unsteady Computations over Two- and Three- Dimensional Bodies,” *43rd AIAA Aerospace Sciences Meeting and Exhibit*, 2005.

[12] Mader, C. A., and R. A. Martins, J. R., “Derivatives for Time-Spectral Computational Fluid Dynamics Using an Automatic Differentiation Adjoint,” *AIAA Journal*, Vol. 50, No. 12, 2012, pp. 2809–2819.

[13] Heeg, J., Chwalowski, P., Schuster, D., and Dalenbring, M., *Overview and Lessons Learned from the Aeroelastic Prediction Workshop*, American Institute of Aeronautics and Astronautics, 2013.

[14] Brooks, A. N., and Hughes, T. J., "Streamline Upwind/Petrov-Galerkin Formulations for Convection Dominated Flows with Particular Emphasis on the Incompressible Navier-Stokes Equations," *Computer Methods in Applied Mechanics and Engineering*, Vol. 32, No. 1, 1982, pp. 199 – 259.

[15] Anderson, W. K., and Bonhaus, D. L., "An Implicit Upwind Algorithm for Computing Turbulent Flows on Unstructured Grids," *Computers & Fluids*, Vol. 23, No. 1, 1994, pp. 1–21.

[16] Biedron, R. T., and Thomas, J. L., "Recent Enhancements to the FUN3D Flow Solver for Moving-Mesh Applications," *AIAA 47th Aerospace Sciences Meeting*, Orlando, Florida, 2009.

[17] Nielsen, E. J., and Anderson, W. K., "Recent Improvements in Aerodynamic Design Optimization on Unstructured Meshes," *AIAA Journal*, Vol. 40, 2002, pp. 1155–1163.

[18] Wang, L., Diskin, B., Biedron, R., Nielsen, E. J., and Bauchau, O., "Sensitivity Analysis of Multidisciplinary Rotorcraft Simulations," *55th AIAA Aerospace Sciences Meeting*, 2017, p. 1670.

[19] Anderson, W. K., Newman, J. C., and Karman, S. L., "Stabilized Finite Elements in FUN3D," *55th AIAA Aerospace Sciences Meeting*, 2017.

[20] Anderson, W. K., and Newman, J., "High-Order Stabilized Finite Elements on Dynamic Meshes," *2018 AIAA Aerospace Sciences Meeting*, 2018.

[21] Allmaras, S. R., Johnson, F. T., and Spalart, P. R., "Modifications and Clarifications for the Implementation of the Spalart-Allmaras Turbulence Model," 2012.

[22] Kiviaho, J. F., Jacobson, K. E., Smith, M. J., and Kennedy, G. J., "A Robust and Flexible Coupling Framework for Aeroelastic Analysis and Optimization," *Proceedings of the 19th AIAA/ISSMO Multidisciplinary Analysis and Optmization Conference*, AIAA, Denver, Colorado, 2017.

[23] Jacobson, K. E., Kiviaho, J. F., Smith, M. J., and Kennedy, G. J., "An Aeroelastic Coupling Framework for Time-Accurate Analysis and Optimization," *Proceedings of the 56th AIAA Aerospace Sciences Meeting*, AIAA, Kissimmee, Florida, 2018.

[24] Wood, S. L., Jacobson, K. E., Jones, W. T., and Anderson, W. K., "Sparse Linear Algebra Toolkit for Computational Aerodynamics," *58th AIAA Aerospace Sciences Meeting*, Orlando, Florida (submitted for publication), 2020.

[25] Smith, M. J., Hodges, D. H., and Cesnik, C. E. S., "Evaluation of Computational Algorithms Suitable for Fluid-Structure Interactions," *Journal of Aircraft*, Vol. 37, No. 2, 2000, pp. 282–294.

[26] Kiviaho, J. F., and Kennedy, G. J., "Efficient and Robust Load and Displacement Transfer Scheme Using Weighted Least Squares," *AIAA Journal*, Vol. 57, No. 5, 2019, pp. 2237–2243.

[27] Jr., C. E. Y., "AGARD Standard Aeroelastic Configurations for Dynamic Response. Candidate Configuration I - Wing 445.6," Tech. Rep. TM-100492, NASA, August 1 1987.

[28] Silva, W. A., Chwalowski, P., and Perry, B., "Evaluation of Linear, Inviscid, Viscous, and Reduced-order Modelling Aeroelastic Solutions of the AGARD 445.6 Wing using Root Locus Analysis," *International Journal of Computational Fluid Dynamics*, Vol. 28, No. 3-4, 2014, pp. 122–139.

[29] *MSC Nastran 2014.1 Release Guide*, MSC Software Corporation, Newport Beach, CA, 2014.

[30] Heeg, J., Wieseman, C., and Chwalowski, P., "Overview and Data Comparisons from the 2nd Aeroelastic Prediction Workshop," 2016.

[31] Chwalowski, P., and Heeg, J., "FUN3D Analyses in Support of the Second Aeroelastic Prediction Workshop," 2016.

[32] Rivera, J., Dansberry, B., Bennett, R., Durham, M., and Silva, W., "NACA 0012 Benchmark Model Experimental Flutter Results with Unsteady Pressure Distributions," AIAA Paper 1992–2396, 1992.

[33] Bennett, R., "Test Cases for Flutter of the Benchmark Models Rectangular Wings on the Pitch and Plunge Apparatus," Tech. Rep. TR ADPO10713, Defense Technical Information Center, March 2000.

[34] Xu, S., Timme, S., and Badcock, K. J., "Enabling off-design linearised aerodynamics analysis using Krylov subspace recycling technique," *Computers & Fluids*, Vol. 140, 2016, pp. 385 – 396.

[35] Karush, W., "Minima of Functions of Several Variables with Inequalities as Side Conditions," Ph.D. thesis, 1939.

[36] Hanson, M. A., "On Sufficiency of the Kuhn-Tucker Conditions," *Journal of Mathematical Analysis and Applications*, Vol. 80, No. 2, 1981, pp. 545–550.